Supporting Information

Atomic-scale Mapping of Dissolution/Deposition Pathways in MnO_2 Polymorphs for Aqueous Zn-MnO_2 Batteries

Chunyu Zhao,[a,c,d] Teng Ma,[a] Ruqian Lian,[c,d] Hongguang Piao, [c,d] Jing Xu, [c,d] Mengqi Wu,[a] Yizhan Wang,[a] Yingjin Wei[a,b,]*

a. Key Laboratory of Physics and Technology for Advanced Batteries (Ministry of Education), College of Physics, Jilin University, Changchun 130012, China.

b. State Key Laboratory of Inorganic Synthesis and Preparative Chemistry, Jilin University, Changchun 130012, China.

c. Department of Physics, College of Science, Yanbian University, Yanji, Jilin 133002, China

d. Institute of Quantum Science and Technology, Yanbian University, Yanji, Jilin 133002, China

Computational Details

This work is based on density functional theory (DFT) calculations using the Vienna Ab-initio Simulation Package (VASP)[1]. The Projector Augmented Wave (PAW)[2] method was employed to describe valence-electron and ion-core interactions, with a plane-wave cut-off energy set to 550 eV. The Perdew-Burke-Ernzerhof (PBE)[3] functional under the generalized gradient approximation (GGA) was used to describe exchange-correlation interactions. The valence electron configurations for pseudopotentials were $3d^{10}4s^2$ for Zn, $3d^5 4s^2$ for Mn, and $2s^2 2p^4$ for O. During geometric optimization, the Brillouin zone was sampled with a K-spacing of 0.4 to ensure a minimum spacing of 0.4 $Å^{-1}$ between adjacent K points. Conjugate gradient algorithms were applied for lattice optimization, with energy and force convergence criteria set to 10^{-6} eV and 0.01 eV $Å^{-1}$, respectively. In addition to spin polarization, the strong correlation effects of Mn-3d orbitals were addressed using the GGA+U method with a U–J parameter of 3.9 eV[4, 5]. To account for van der Waals (vdW) dispersion interactions between MnO_2 layers, the DFT-D3 method proposed by Grimme was incorporated[6]. For surface property calculations, we constructed a thick plate-like model to ensure that the bulk phase properties are restored in the intermediate layer. The specific number of layers varies depending on the crystal plane, but typically includes 6 to 8 atomic layer. The lateral size (x-y plane) of the surface model is 8 Å×8 Å at least in surface calculation. a 20 Å vacuum layer was constructed along the surface normal to eliminate interactions between periodic slabs. A relaxation scheme fixing the bottom atomic layers while allowing surface atoms to relax was adopted to ensure accurate determination of intrinsic surface characteristics.

In this study, the spin-orbit coupling effect was not included. This is because for the 3*d* transition metal oxides (with Mn atomic number 25) that we are investigating,

the SOC effect usually has a relatively small impact on the total energy, geometric structure, and the reaction energy we are concerned with (ΔG), especially when comparing the relative energies of materials in the same series (different MnO_2 polymorphs). For surface calculations, dipole correction was applied to eliminate the false dipole interactions caused by periodic boundary conditions.

To investigate the desolvation behavior of Mn^{2+} in electrolytes, the Gaussian 09[7] quantum chemistry software package was used to systematically simulate the stepwise desolvation processes of $Mn(H_2O)_6^{2+}$ and $Mn(OH)_6^{4-}$. The B3LYP (Becke–Three–parameter–Lee–Yang–Parr)[8] hybrid functional was applied for exchange-correlation interactions, incorporating semi-empirical DFT-D3 dispersion corrections and spin polarization[9]. The 6-31G(d) basis[10] set was used for geometric optimization, while single-point energy calculations employed the extended 6-31+G(d) basis set[11]. To account for solvent effects, the Solvation Model based on Density (SMD) implicit solvation model was implemented throughout all calculations[12].

Formation Enthalpy Calculation: The formation enthalpy (*ΔH*) of polymorphic MnO_2 and reaction products from solid-solid transformation mechanisms involving H^+ and Zn^{2+} intercalation/deintercalation mechanisms was calculated using the formula:

$$\Delta H = H_P - H_R \quad (1)$$

where H_P and H_R represent the enthalpy of the products and reactants, respectively. A more negative *ΔH* indicates greater thermodynamic stability of the product.

Gibbs Free Energy Calculation: The Gibbs free energy change (*ΔG*) of bulk MnO_2 during different reaction mechanisms and surface dissolution/deposition processes was calculated via the formula[13]:

$$\Delta G = \Delta E_S + \Delta E_{ZPE} - T\Delta S \quad (2)$$

where $\Delta E_S$is the energy difference of the system before and after the

reaction, T=298.15K (room temperature), ΔS is the entropy change, and ΔE_{ZPE} is the zero-point energy. The zero-point vibrational energy (ZPE) and entropy (S) are obtained by calculating the vibration frequencies for gaseous molecules (O_2, H_2O), ions (H^+, Zn^{2+}, Mn^{2+}) and solid substances. For solid substances, we used the finite displacement method to calculate the phonon spectrum, from which we obtained ZPE and vibrational entropy. For ions and molecules, we performed frequency calculations in Gaussian 09 using the B3LYP-D3/6-31+G(d) level and the SMD solvation model. The Gibbs free energy G = H - TS, where H is the enthalpy (EDFT + ZPE). Regarding the determination of entropy, specifically, the vibrational entropy of solid substances is derived from phonon calculations. For gaseous species (O_2, H_2O), the entropy includes translational, rotational and vibrational contributions, which are obtained from frequency calculations. For hydrated ions (such as Mn^{2+}(aq)), we calculated their vibrational entropy in the implicit solvent model (SMD), but it should be noted that in the SMD model, translational and rotational degrees of freedom are suppressed, so the calculated entropy mainly reflects the vibrational contribution and the constraint brought by solvation effects, which is different from the entropy value of standard gaseous molecules.

Redox Potential Calculation: The redox potential (V) of MnO_2 under different mechanisms was determined using the formula[14]:

$$V = -\frac{\Delta G}{nF} \tag{3}$$

where ΔG is the Gibbs free energy change of the polymorphic MnO_2 during the reaction, n is the number of transferred electrons, and F is the Faraday constant

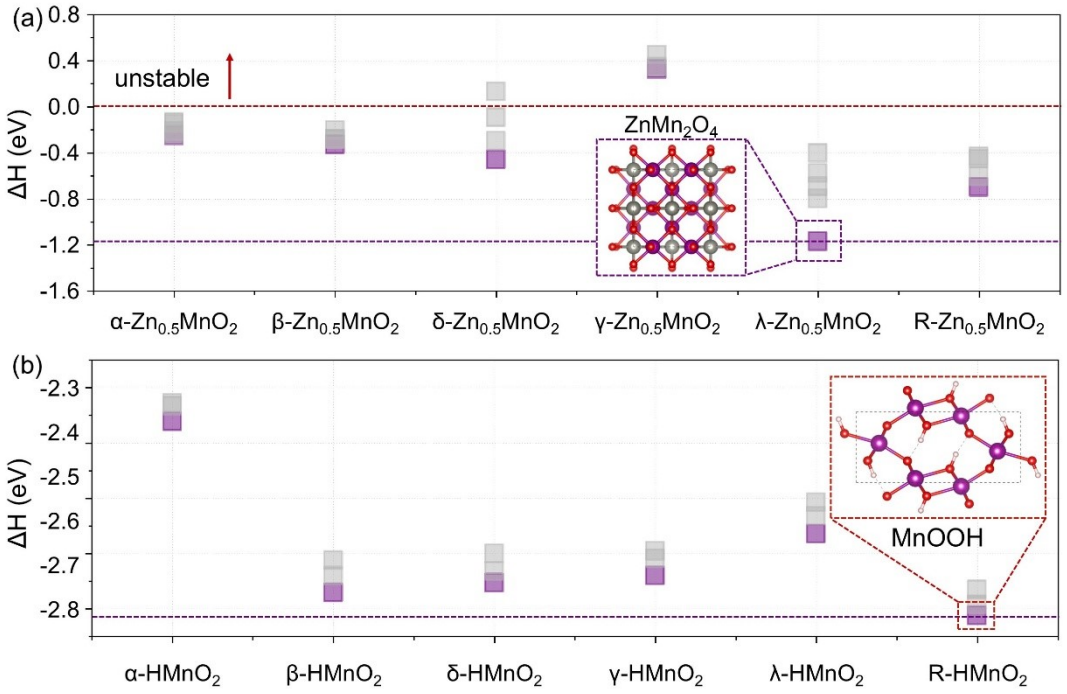

Fig. S1 Discharge products in (a) the Zn^{2+} involved redox reaction of MnO_2 cathode through the insertion/extraction mechanism, and (b) the H^+ involved redox reaction of MnO_2 cathode via the solid-solid conversion mechanism.

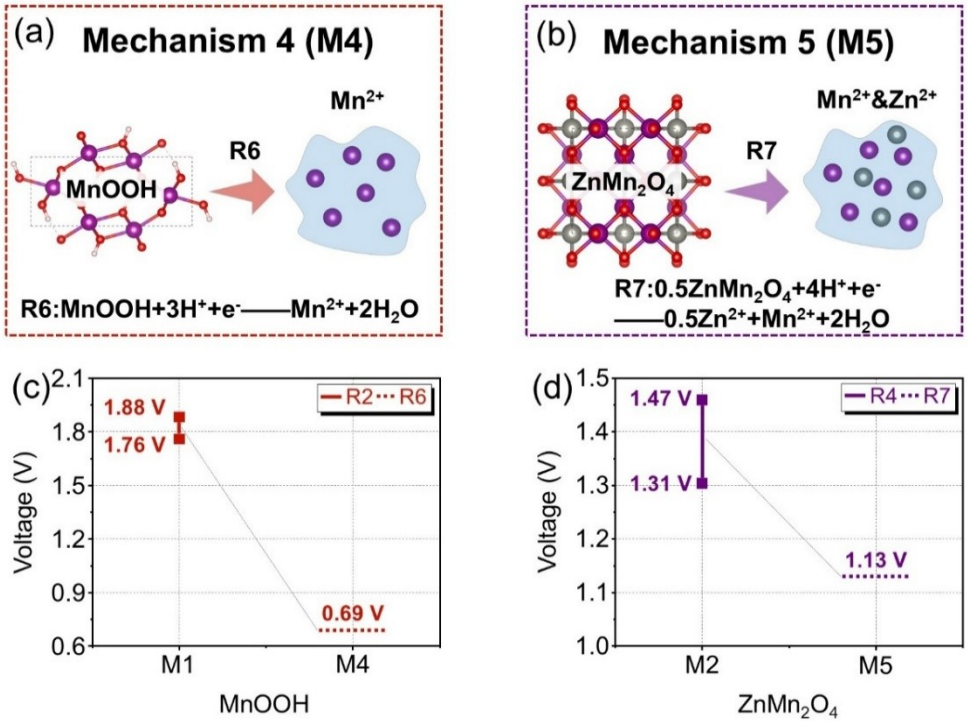

Fig. S2 Dissolution/deposition mechanism of (a) MnOOH and (c) $ZnMn_2O_4$, and corresponding redox potential of (b) MnOOH and (d) $ZnMn_2O_4$.

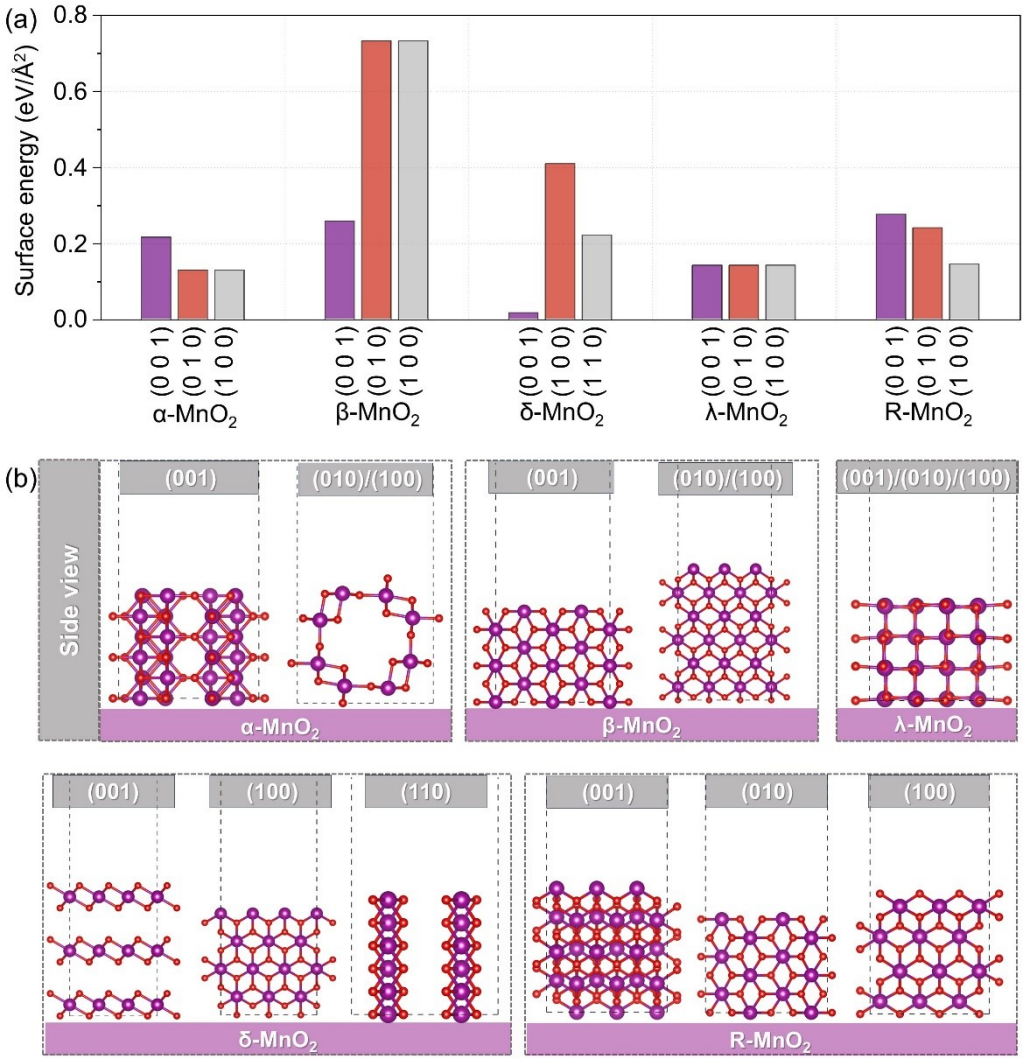

Fig. S3 (a) The surface energy of low-Miller-index facets for five MnO_2 crystal forms, and (b) their corresponding surface atomic structures.

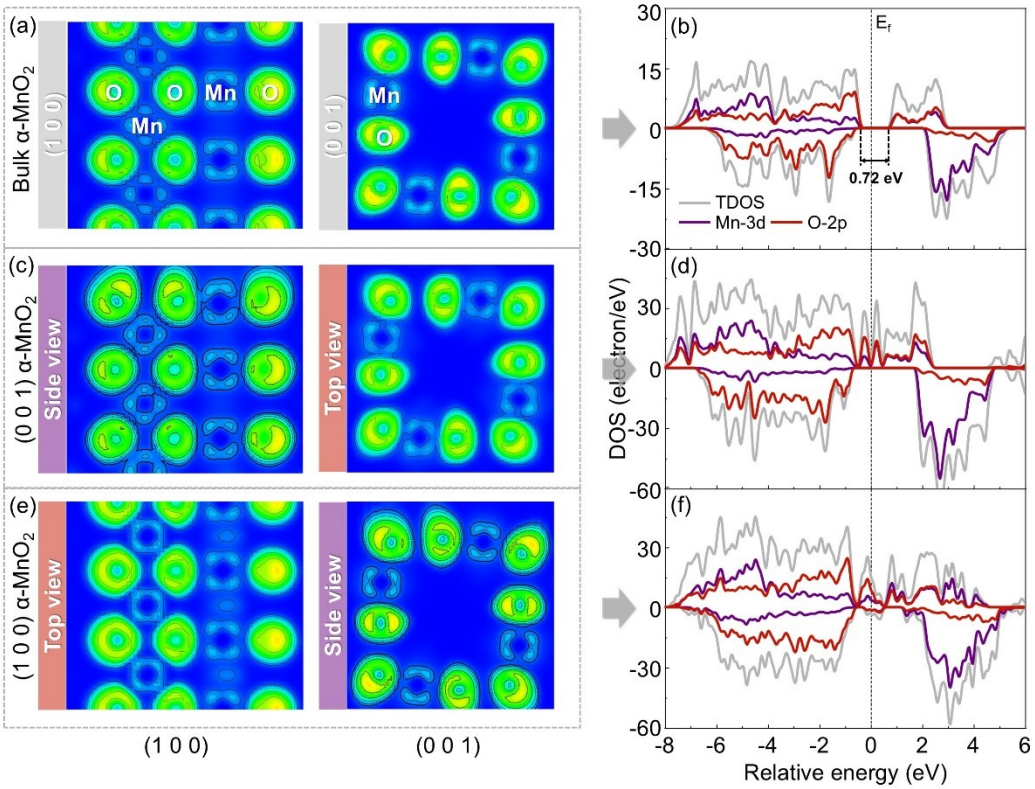

Fig. S4 The electron local function and electron state density of α-MnO_2 bulk phase and its different crystalline orientation surface.

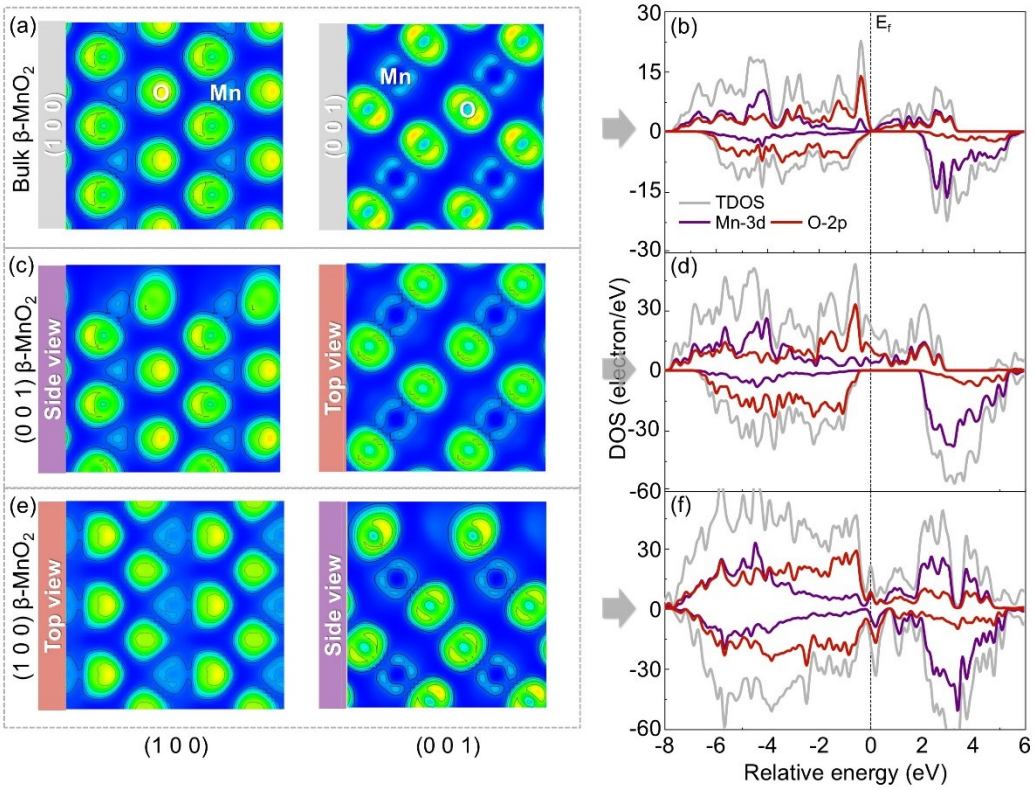

Fig. S5 The electron local function and electron state density of β-MnO_2 bulk phase and its different crystalline orientation surface.

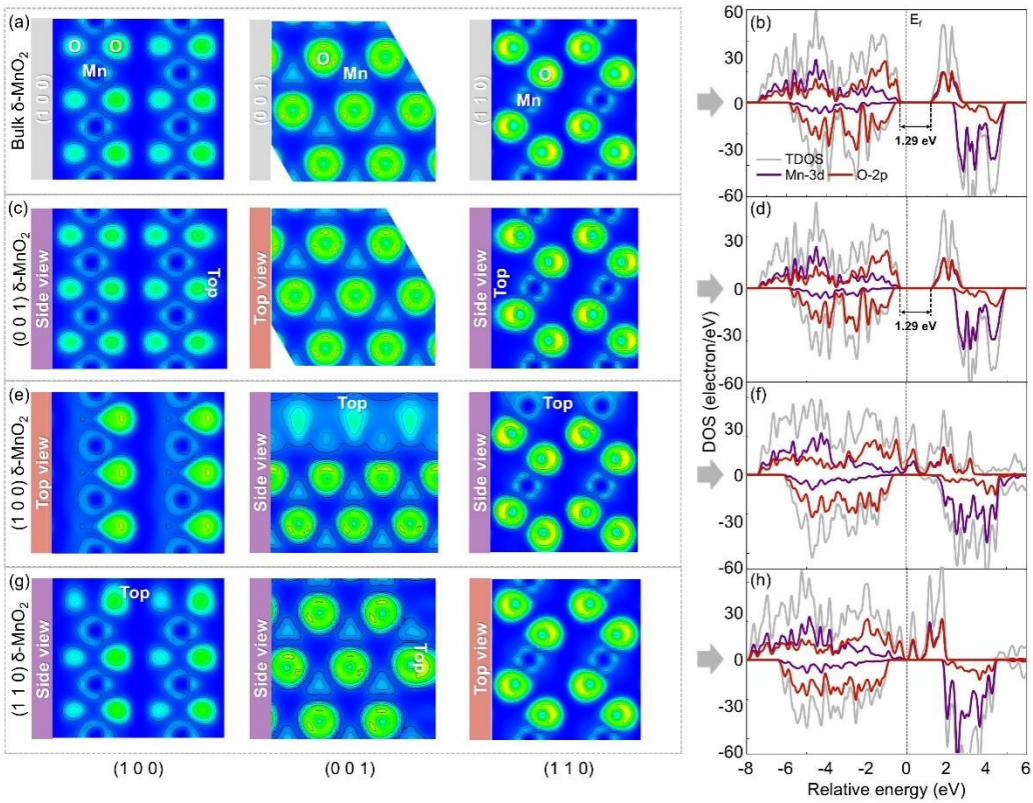

Fig. S6 The electron local function and electron state density of δ-MnO_2 bulk phase and its different crystalline orientation surface.

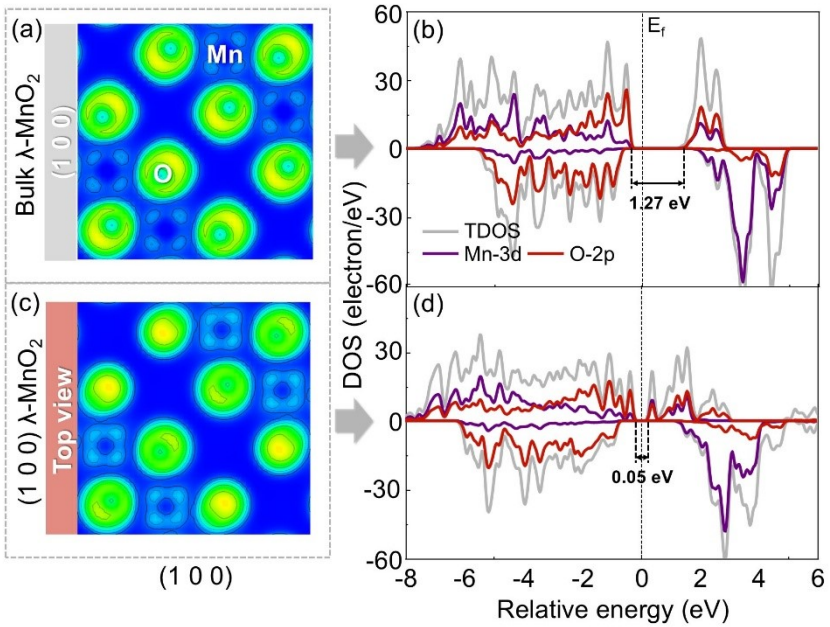

Fig. S7 The electron local function and electron state density of λ-MnO_2 bulk phase and its different crystalline orientation surface.

References

1. G. Kresse and J. Furthmüller, *Physical Review B*, 1996, **54**, 11169-11186.
2. G. Kresse and D. Joubert, *Physical Review B*, 1999, **59**, 1758-1775.
3. J. P. Perdew, K. Burke and M. Ernzerhof, *Physical Review Letters*, 1996, **77**, 3865-3868.
4. L. Wang, T. Maxisch and G. Ceder, *Physical Review B*, 2006, **73**, 195107.
5. M. Liu, Z. Rong, R. Malik, P. Canepa, A. Jain, G. Ceder and K. A. Persson, *Energy & Environmental Science*, 2015, **8**, 964-974.
6. S. Grimme, J. Antony, S. Ehrlich and H. Krieg, *The Journal of Chemical Physics*, 2010, **132**, 154104.
7. M. J. Frisch, G. W. Trucks, H. B. Schlegel, G. E. Scuseria, M. A. Robb, J. R. Cheeseman, G. Scalmani, V. Barone, G. A. Petersson, H. Nakatsuji, M. C. X. Li, A. Marenich, J. Bloino, B. G. Janesko, R. Gomperts, B. Mennucci, H. P. Hratchian, J. V. Ortiz, A. F. Izmaylov, J. L. Sonnenberg, D. Williams-Young, F. L. F. Ding, J. G. F. Egidi, A. P. B. Peng, T. Henderson, D. Ranasinghe, V. G. Zakrzewski, N. R. J. Gao, G. Zheng, W. Liang, M. Hada, M. Ehara, K. Toyota, R. Fukuda, J. Hasegawa, M. Ishida, T. Nakajima, Y. Honda, O. Kitao, H. Nakai, T. Vreven, K. Throssell, J. A. Montgomery, Jr., J. E. Peralta, F. Ogliaro, M. Bearpark, J. J. Heyd, E. Brothers, K. N. Kudin, V. N. Staroverov, T. Keith, R. Kobayashi, J. Normand, K. Raghavachari, A. Rendell, J. C. Burant, S. S. Iyengar, J. Tomasi, M. Cossi, J. M. Millam, M. Klene, C. Adamo, R. Cammi, J. W. Ochterski, R. L. Martin, K. Morokuma, O. Farkas, J. B. Foresman and D. J. Fox, *Journal*, 2009.
8. C. Adamo and V. Barone, *The Journal of Chemical Physics*, 1999, **110**, 6158-6170.
9. S. Grimme, S. Ehrlich and L. Goerigk, *Journal of Computational Chemistry*, 2011, **32**, 1456-1465.
10. M. M. Francl, W. J. Pietro, W. J. Hehre, J. S. Binkley, M. S. Gordon, D. J. DeFrees and J. A. Pople, *The Journal of Chemical Physics*, 1982, **77**, 3654-3665.
11. A. D. Becke, *The Journal of Chemical Physics*, 1993, **98**, 5648-5652.
12. J. Tomasi, B. Mennucci and R. Cammi, *Chemical Reviews*, 2005, **105**, 2999-3094.
13. S. Kosasang, N. Ma, P. Wuamprakhon, N. Phattharasupakun, T. Maihom, J. Limtrakul and M. Sawangphruk, *Chemical Communications*, 2018, **54**, 8575-8578.
14. G. Yoon, D.-H. Kim, I. Park, D. Chang, B. Kim, B. Lee, K. Oh and K. Kang, *Advanced Functional Materials*, 2017, **27**, 1702887.